Effect of Laser Scribing on Coating, Drying, and Crystallization of Absorber Layer of Perovskite Solar Cells

Chaopeng Huang, Cheng-Kang Guan, Bo-Qian Lin, Shih-Han Huang, Bin-Juine Huang, Wei-Fang Su, and Li Xu*

Large-area perovskite solar modules fabrication has been demonstrated with a rapid process of large-area slot-die coating, drying, and crystallization using near-infrared radiation in ambient air, in which the laser-scribing process is applied to fabricate the modules. However, defective coating of perovskite layer near laser-scribed P1 line which isolates the front electrode of transparent conductive oxide (TCO) results very low module efficiencies. Therefore, systematic study is conducted to investigate the root cause, mechanism and solution of the defective coating and crystallization of the perovskite layer. Scanning electron microscope, energy-dispersive X-ray spectroscopy, and atomic force microscopy are used to characterize the TCO film before and after P1 scribing. It is found that P1 laser-scribing process changes surface morphology of TCO at the area near P1 line, which decreases the surface wettability and results discontinuous coating of precursor solution near P1 lines. The absence of TCO material in the P1 trench induces nonuniform heating during NIR annealing step, which is verified by thermal analysis via numerical simulation. After tuning laser process recipes, a large module with an active area of 46 cm^2 is fabricated with a power conversion efficiency of 7.2% and geometry fill factor of 93.8%.

1. Introduction

Recently, perovskite solar cells (PSCs) have shown high potential for next-generation solar cells owing to their high power conversion efficiency (PCE) and low fabrication cost. For example, in 2021, a single-junction PSC with an impressive PCE of 25.6% was reported by Jeong et al.[1] Meanwhile, the development of scalable coating techniques such as D-bar coating,[2] spray coating,[3] inkjet printing,[4] screen printing,[5] blade coating,[6] and slot-die coating[7] is also proposed to enable commercialization of large-area cells with high-efficiency PSCs. In addition,

vacuum treatment,[8] heat treatment[9] and nitrogen blowing,[10] near-infrared radiation (NIR),[11] and other scalable annealing processes have been investigated to control the morphology and improve the crystallization quality of perovskite layers.

Large-area fabrication of perovskite solar modules (PSMs) requires an integration process to connect small-area PSCs in series. Monolithically series-interconnected structure with patterning line process, P1, P2, and P3, is widely used in thin-film solar modules. As demonstrated in **Figure 1**, P1 isolates the front electrode of each subcell. P2 removes all the functional layers, including the electron transport layer (ETL), absorbing layer, hole transport layer (HTL), and work function modify layer (WFL), allowing the back electrode directly contact the front electrode. P3 separates the back electrode. The region between the patterning lines is called the dead area, which cannot contribute to photo-generated current, and is evaluated with a geometry fill factor (GFF) defined as the ratio of the active area to the aperture area. Several patterning technologies have been developed, such as mask pasting,[12] chemical etching,[13] mechanical scribing,[14] and laser scribing.[15] Laser scribing is a winning candidate with many advantages, such as high scribing precision, selectively removing different layers based on selective absorption of laser light, and no residual stress left since it is a noncontact process. Many research efforts have been applied in using ultra-fast lasers (picosecond and femtosecond lasers) in the scribing processes of thin-film solar module fabrication, which significantly increase the fabrication cost.[16] Our recent work showed that nanosecond pulsed laser also could fabricate high-efficiency PSMs with high repeatability and low cost.[17]

In the effort to apply the laser-scribing technology on large area module fabrication by all slot-die coating with rapid NIR heating in ambient air, we found that the laser scribing of TCO layer (P1) often causes problems with a slot-die coating of precursor solution around the P1 line, and further crystallization of perovskite layer near P1 line during NIR annealing. Nanosecond pulse lasers, compared with picosecond lasers, tend to create crater-like film morphology, resulting in an undesirable rough coating. Furthermore, after the laser P1 process, the de-wetting phenomenon often occurred in the subsequent coating processes, that is, the solution flowing away from the

C. Huang, C.-K. Guan, B.-Q. Lin, B.-J. Huang, L. Xu
Department of Mechanical Engineering
National Taiwan University
Taipei 106, Taiwan
E-mail: lixus@ntu.edu.tw

S.-H. Huang, W.-F. Su
Department of Material Science and Engineering
National Taiwan University
Taipei 106, Taiwan
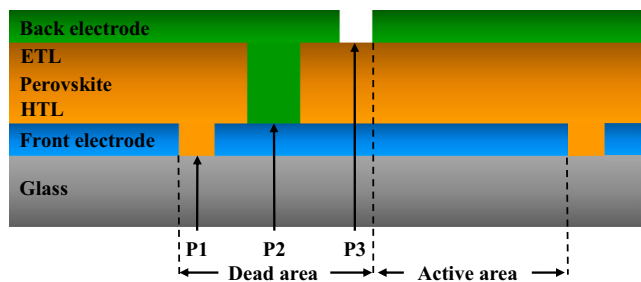
Figure 1. Schematic cross-sectional view of a monolithically series-interconnected structure.

P1 line, especially for perovskite precursor solution with high surface tension solvents such as dimethyl sulfoxide (DMSO), γ-butyrolactone (GBL), and N,N-dimethylformamide.[6d] In the subsequent NIR lamp heating process, precursor films around P1 lines transformed into films with different grain structures than regular perovskite layers in other areas. As a result, discontinuous films and poor-quality perovskite films around the P1 line were often observed in the module fabrication process, as shown in **Figure 2**, resulting in a low fill factor and low PCE.

In this study, we conducted experiments to find the root cause of the effect of laser-scribing P1 on the coating and crystallization of the perovskite layer. Scanning electron microscope (SEM), energy-dispersive X-ray spectroscopy (EDS), and atomic force microscope (AFM) are used to characterize the TCO film before and after P1 scribing. Furthermore, we identified the root cause of the abnormal crystallization of the perovskite layer during NIR annealing, which was verified by thermal analysis via numerical simulation. Finally, the large-area PSMs were successfully fabricated with decent PCEs.
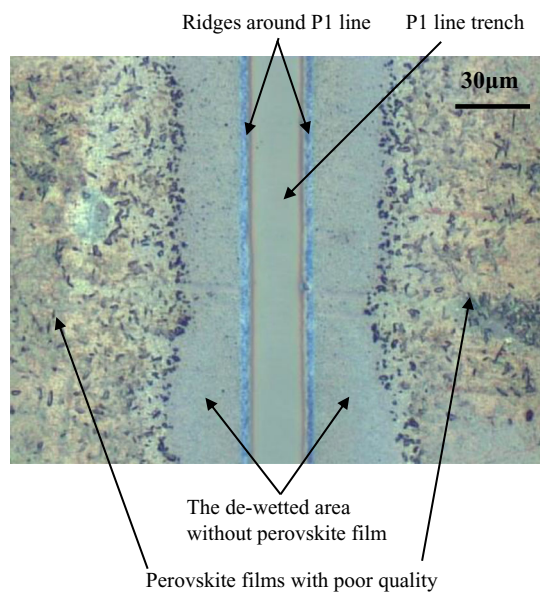
Figure 2. Optical microscope (OM) image of the discontinuous perovskite films with poor quality around P1 line.

2. Results and Discussion

The laser pulse width of a few nanoseconds is selected based on our previous work, which aims to lower the manufacturing cost by developing all laser processes to fabricate large-area perovskite modules with nanosecond pulsed laser instead of picosecond laser and femtosecond laser that are often reported.

The morphology of the scribing line is affected by many factors, such as the laser wavelength, output power, beam size, scan speed, and overlap ratio. Here, we applied the selective laser processing of multiple layers. According to Beer–Lambert law, when monochromatic radiation is passed through a medium, the intensity of the transmitted radiation decreases with the increase in the thickness of the absorbing medium, and it varies directly with the incident radiation. The ability of a material to absorb light is defined as its absorption coefficient. Materials have different absorption coefficients for different wavelengths of light. Thus, choosing the correct laser wavelength is essential to achieve selective laser processing of multiple layers. For example, perovskite has a very high absorption coefficient to visible light. Thus, a green light laser with a wavelength of 532 nm can effectively remove the perovskite layer without damaging fluorine-doped tin oxide (FTO) in the P2 scribing process. FTO has low absorption to 532 nm laser light; much higher energy is needed to ablate the FTO in the P1-scribing process. Generally, we can increase the output power and decrease the beam size to obtain higher power density.

The overlap ratio, defined in Equation (1), can also adjust the laser energy absorbed at each position. The higher the overlap ratio, the more energy the region accumulates and is absorbed. By adjusting laser-scribing parameters, we can control the width, depth, and surface morphology of scribing lines to adjust the effect of scribed lines on the subsequent coating and annealing process.

$$\text{Overlap Ratio}(\%) = 100 * \left(1 - \frac{\text{Scan Speed}(\frac{m}{s})}{\text{Repetition Rate}(\frac{1}{s}) * \text{Spot Diameter}(m)}\right) \quad (1)$$

2.1. Laser Scribing of P1

The resistance across the P1 was measured with an Avometer after laser scribing, and the value is higher than several megohms, indicating full electrical insulation of the neighboring cells. Two sets of P1 parameters were applied to investigate the effect of P1 on the subsequent coating and annealing process. The first recipe was to set the laser with a defocus length of 150 μm. With the same output power, the spot size increased when the laser was defocused, resulting in a smaller power density of $1.8 \times 10^8\,\text{W cm}^{-2}$ and an overlap ratio of 95.6%. The second recipe was to set the sample surface strictly at the laser focal plane resulting in an increased power density of $2.4 \times 10^8\,\text{W cm}^{-2}$ and an overlap ratio of 93.3%. Line width is defined as the distance between the highest point of the raised edge of P1. The line widths of P1 scribed with the two recipes were 30 and 20 μm, respectively; thus, the two recipes were named P1–30 and P1–20 μm.

P1 scribing of the FTO layer is a laser ablation process. If the pulse duration is shorter than the electron cooling time, typically a few picoseconds, a natural solid-to-vapor transition occurs.[20] However, a solid–liquid–vapor process occurs if the pulse duration is on the order of nanoseconds. Nevertheless, if the laser energy is insufficient to melt and evaporate the materials, a crater-shaped heat-affected zone is generated.[21] The ablated material would be redeposited as particles on FTO film, which increased the roughness of the FTO film around the P1 region. OM images of P1 lines by laser recipes of P1–30 and P1–20 μm are shown in **Figure 3**a,b, respectively. The area beside the P1 lines showed a slightly different reflection. To verify the surface condition change, we measured contact angles between the FTO film and perovskite precursor solution, FTO patterned with P1–30 μm and perovskite precursor solution, and FTO patterned with P1–20 μm and perovskite precursor solution. As shown in Figure 3c, the contact angle between the standard FTO film and precursor solution is 27.73°, whereas the contact angles between the FTO film patterned with P1 line and precursor solution are 32.01° and 38.12° for recipe P1–20 and P1–30 μm, respectively. P1 process increases the contact angle, indicating that the wettability of precursor solution to the FTO surface is reduced. Recipe P1–30 μm showed a larger contact angle than recipe P1–20 μm, suggesting redeposition of more ablated material, thus weaker wettability to perovskite precursor. A schematic diagram of the measuring area and the camera's location is shown in Figure 3d.

AFM is used to analyze the surface morphology change of the FTO film after P1 scribing. **Figure 4**a,b demonstrates the 3D morphology of the P1 line and the peripheral area, including the heat-affected zone and the area with redeposition. The roughness (R_a) of the FTO surface significantly increased from 14.2 to 19.9 nm and 25.9 nm after P1 scribing by recipe P1–30 and P2–20 μm, respectively, as shown in **Table 1**, which verifies the existence of redeposited material after laser scribing and suggests that more material was redeposited by recipe P1–30 μm compared to recipe P2–20 μm. Figure 4c is the 2D profile of P1 lines. A crater-shaped morphology was observed at the edge of P1–30 μm, with a ridge height of around 300 nm. However, the ridge was barely seen at the edge of the P1–20 μm cases. During the laser ablation process, the energy at the edge of the laser beam is not enough to completely melt and evaporate the material; instead, the material melts and resolidifies and forms ridges at the edge. However, if the laser energy is much more concentrated when the laser is focused (i.e., recipe P1–20 μm), the ablation process results in a much smoother edge attributed to the higher gradient of laser intensity profile at the edge inducing smaller molten zone; thus less material is melted
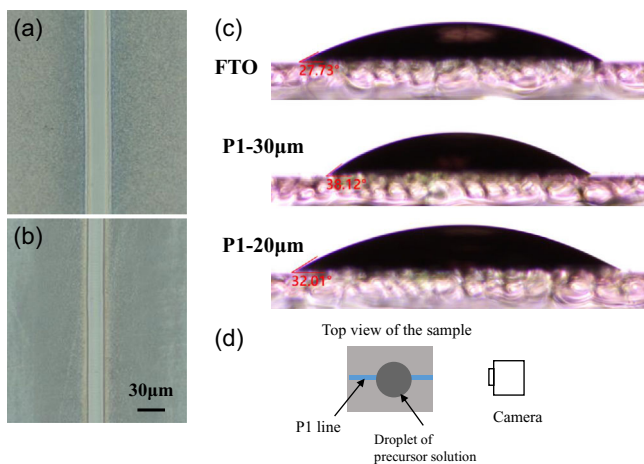
Figure 3. Images of OM of laser-scribed FTO substrate with a) recipe P1–30 μm and b) recipe P1–20 μm. c) Contact angles of perovskite precursor solution on different FTO substrates; d) Schematic diagram of the contact angle measurement setup.
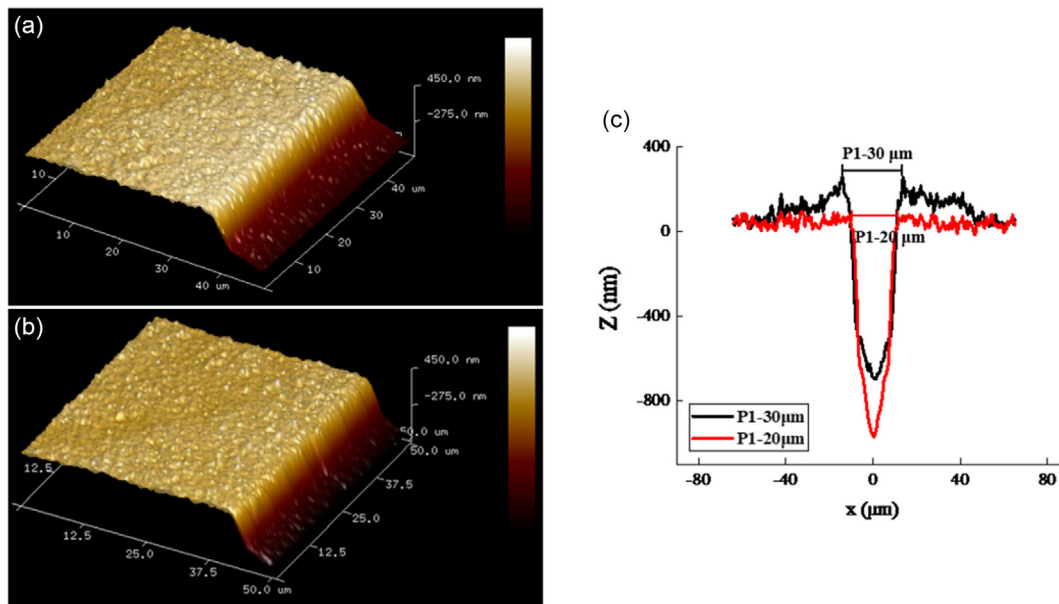
Figure 4. The 3D atomic force microscope (AFM) profile of a) P1–30 μm and b) P1–20 μm. c) The 2D AFM profile of P1–30 and P1–20 μm.

Table 1. Contact angle and surface roughness of the surrounding area of P1 line.

Parameter	P1–30 μm	P1–20 μm	FTO
Average roughness R_a	25.9 nm	19.9 nm	14.2 nm
Average roughness R_q	31.2 nm	24.9 nm	18.1 nm
Contact angle	38.1°	32.0°	27.7°

and solidifies. Comparing recipe P1–20 and P1–30 μm, the latter showed higher roughness at the area around P1 and generated ridges at the edge of the scribing line, which would cause higher defects during slot-die coating and crystallization by NIR heating.

2.2. Thermal Analysis of the Heating Process

Another possible reason that causes the abnormal crystallization of perovskite film is the lower-temperature and high-temperature gradient of films around the P1 region during the NIR process. FTO film strongly absorbs photon energy from the infrared lamp and converts it to thermal energy, and the FTO film with elevated temperature then heats the top precursors through thermal conduction, which induces crystallization and formation of the perovskite layer. As P1 scribing removes the FTO, the absence of FTO results in no heat generation in the P1 trench, which means the temperature of the precursor in and around the P1 line is different from other areas. To figure out the temperature profile, numerical simulation was performed with finite element analysis (FEA). The numerical model is shown in **Figure 5**a, a
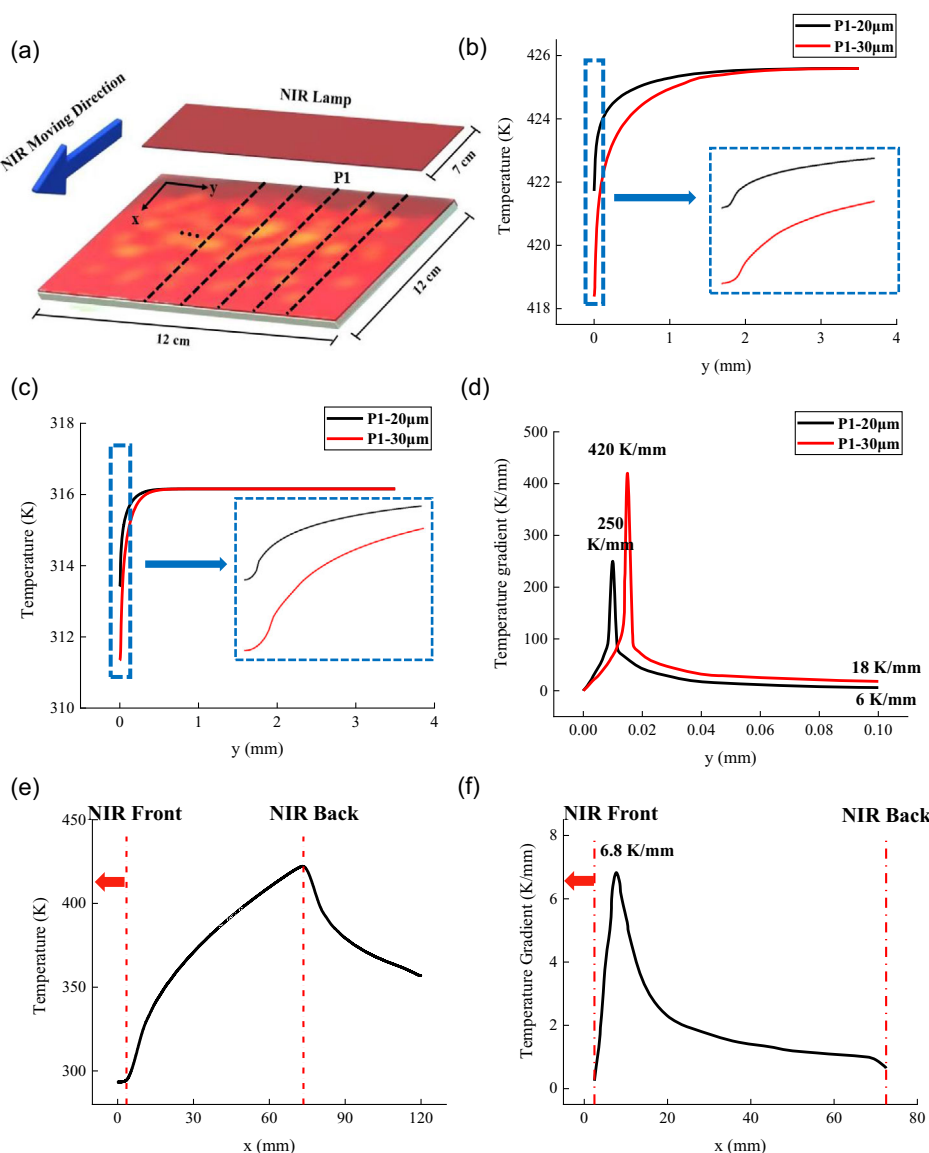

Figure 5. a) Schematic diagram of near-infrared radiation (NIR) heating process; b) temperature distribution in the *y*-direction at the end of NIR irradiation; c) temperature distribution in the *y*-direction when the film is just exposed to NIR irradiation; d) temperature gradient of (c); e) temperature distribution at the center of P1 line in the *x*-direction; f) temperature gradient of (e).

12×12 cm glass coated with FTO film is heated by an NIR lamp moving with a constant speed in the x-direction, and the P1 line is also in the x-direction. Figure 5b shows the temperature profile along the y-direction, which is perpendicular to the P1 line at the end of NIR irradiation, and the center of the P1 line is set at the position of $y = 0$. The temperature in and around the P1 line is lower than that of regions at a distance. The two curves showed a temperature difference of 7.2 K for recipe P1–30 μm and 3.8 K for recipe P1–20 μm, indicating a broader P1 leads to a higher temperature difference. Figure 5c,d shows the temperature distribution and temperature gradient in the y-direction when the film was exposed to the moving NIR lamp or at the heating front. The temperature gradient in (d) was calculated by taking the first derivative of the temperature profile in Figure 5c. The maximum temperature gradient locates at the edge of P1, which is the cut-off point with or without light absorption. The maximum value of temperature gradient for P1–30 and P1–20 μm is 420 and 250 K mm^{-1}, respectively. Temperature distribution and temperature gradient along the x-direction are shown in Figure 5e,f. Temperature increases along the moving direction and reaches the maximum at the end of the exposure process. The temperature gradient at the center of P1 in the x-direction showed a maximum value of 6.8 K mm^{-1}, which is two orders of magnitude lower than the y-direction. Thus, the temperature gradient in the y-direction is the main driving force of the film rupture. Broader P1 results in a higher-temperature gradient in the

y-direction and increases the possibility of film rupture. In addition, broader P1 also leads to a larger temperature difference between the surrounding region of P1 and far away, which may result in poor crystallization near P1. Thus, the linewidth of P1 has a crucial effect on the film coating and crystallization of perovskite layers when using rapid NIR heating. Further reduction of the linewidth of P1 helps improve the quality of perovskite films.

2.3. Laser Scribing of P2

P2 needs to completely ablate HTL, perovskite, ETL, and WFL without damaging FTO to minimize the internal loss of PSMs. Contact resistance was measured by transfer line method (TLM), as shown in **Figure 6**a,b. The contact resistance between FTO, NiO$_x$, and Ag is 6.9 Ω, while if there is no Ni left, the contact resistance is only 1.4 Ω. The residual NiO$_x$ layer would significantly increase the series resistance, leading to the module's internal loss. After laser scribing, EDS analysis was applied to detect residual elements on the P2 line. As shown in Figure 6c,d, in the middle of P2, the atomic ratio of Ni is always close to 0, indicating that NiO$_x$ is entirely removed by laser. A contact width is defined as the width where there is no NiO$_x$ left in the P2 trench, and it is 55 μm in this case, smaller than the line width of 95 μm, including the heat-affected zone. Meanwhile, there is no sudden drop in the atomic ratio of Sn or sudden
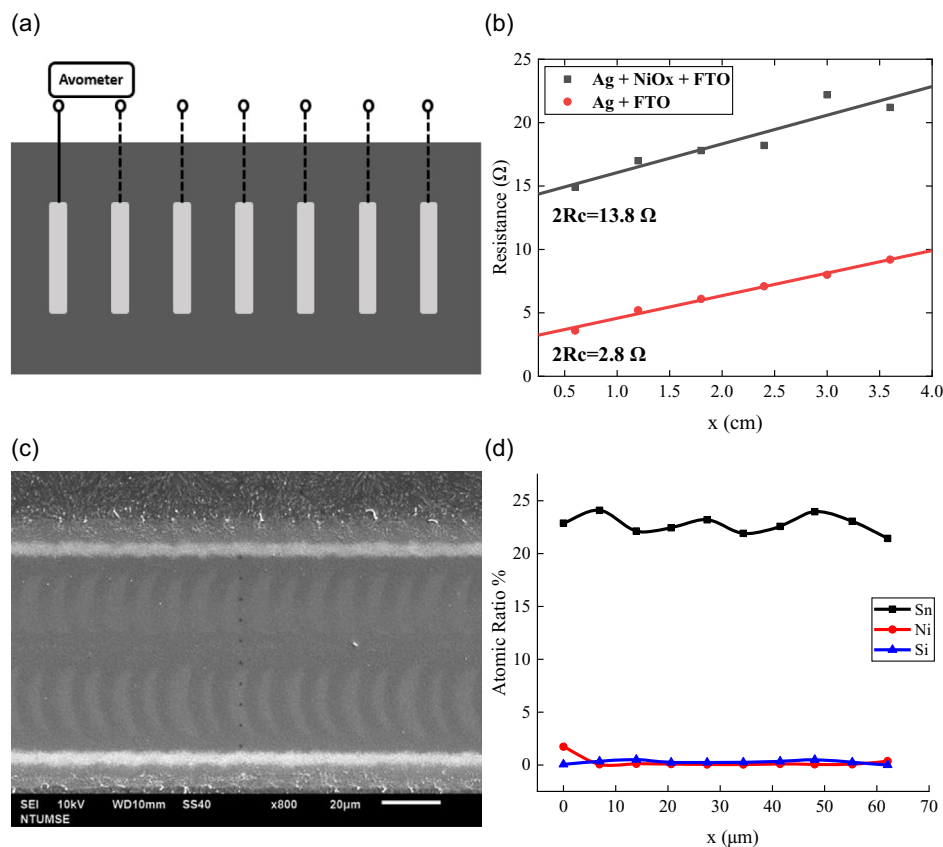
Figure 6. a) Schematic diagram of transfer line method (TLM) measurement. b) The contact resistance of Ag/FTO and Ag/NiO$_x$/FTO. c) Scanning electron microscope (SEM) image of P2 and d) energy-dispersive X-ray spectroscopy (EDS) analysis of P2.

increase in the atomic ratio of Si, which means there is no damage to the FTO and glass substrate throughout the P2 region.

2.4. Laser Scribing of P3

The last procedure in PSMs fabrication is P3. The residual electrode material may lead to a short circuit. As demonstrated in **Figure 7**, no residual Ag was detected in the P3 line, indicating that the adjacent cells were completely insulated by laser scribing. Meanwhile, only a weak signal of Pb and Ni was detected, suggesting that most of the perovskite and NiO_x were also ablated. The atomic ratio of Sn does not decrease significantly, whereas the atomic ratio of Si does not increase, indicating that the laser did not damage the FTO layer in the P3 trench. Moreover, the SEM image showed the Ag curl outward at the edge of P3 and will not contact the exposed FTO in the P3 line. Direct contact of the top and bottom electrodes may lead to a severe shunting problem. Thus, P3 scribing in this study can entirely insulate the back electrode without shunting.

2.5. Module Fabrication and Evaluation

To investigate the effect of P1 on module PCE, FTO substrates patterned with P1–30 and P1–20 μm were used to fabricate mini
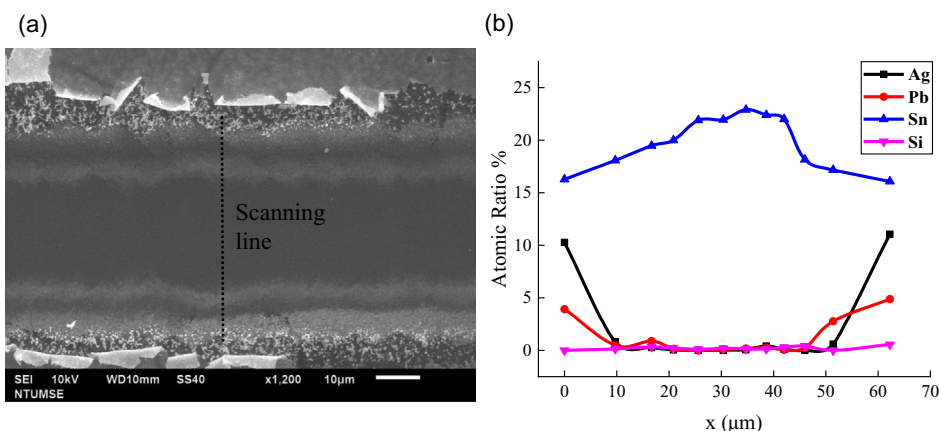
**Figure 7.** a) SEM image of P3. b) EDS analysis of P3.
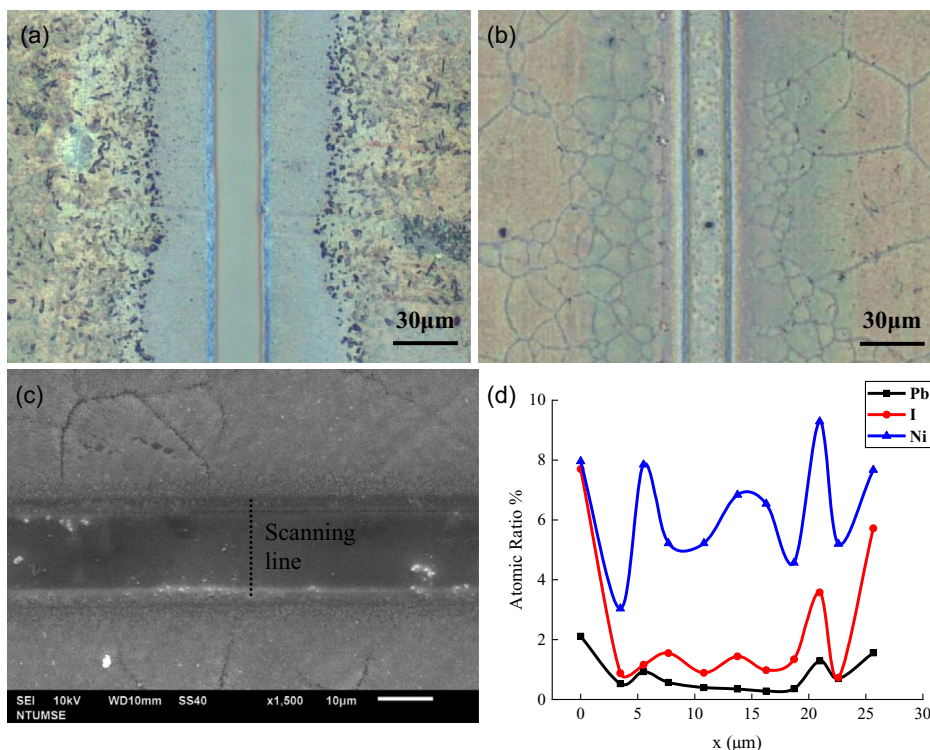
Figure 8. OM images after slot-die coating and NIR heating of the areas showing a) discontinuous perovskite film with poor quality by recipe P1-30 μm and b) continuous perovskite film with good quality by recipe P1-20 μm. c) SEM image of (b). d) EDS analysis of the scanning line in (c).

PSMs. **Figure 8**a shows that when using FTO patterned with P1–30 μm to fabricate modules, P1 was not covered by perovskite. As discussed earlier, a large temperature gradient in the P1 region may lead to film rupture when rapid NIR irradiation is applied. In addition, P1–30 μm has poorer wettability to perovskite precursor; thus, defects are more likely to occur during the slot-die coating process. When using P1–20 μm to fabricate modules, no rupture was observed. Figure 8b shows that crystallized perovskite completely covers the area surrounding P1. Narrower P1 produces a smaller temperature gradient, combined with a smoother surface; a process window exists to obtain a dense and crystallized perovskite film under rapid NIR irradiation. EDS analysis was also applied to detect the residual element of P1, as shown in Figure 8c,d. A Pb signal exists in P1–20 μm, which means perovskite completely covers the whole P1 region.

The performance of PSMs fabricated by the two P1 recipes is shown in **Figure 9**. Recipe P1–20 μm gives better values than recipe P1–30 μm in all aspects. **Figure 10** shows the current density–voltage (*J–V*) curve of the control sample (0.09 cm^2) and champion PSM fabricating with two recipes. All module performances in this study are based on the active area. The average PCE of 8 modules fabricated with P1–30 μm is 2.5%, while the champion PCE is 3.2%. The main reason for limiting the module PCE is the low fill factor. Due to the fracture of the perovskite layer, the HTL contacts directly with the ETL at the surrounding area of P1, leading to a severe shunting problem. The average PCE of 12 modules fabricated with P1–20 μm is 7.3%, and the average fill factor

is above 50%. No significant shunt was observed since the P1 area was entirely covered by perovskite film. The champion module's PCE is 8.3%, based on an active area of 13.4 cm^2, close to the control sample. As shown by the red and blue lines in Figure 10, the efficiency loss from a small cell to a large-area module mainly comes from the open circuit voltage. The average V_{oc} for each cell can steadily achieve over 0.9 V, but still lower
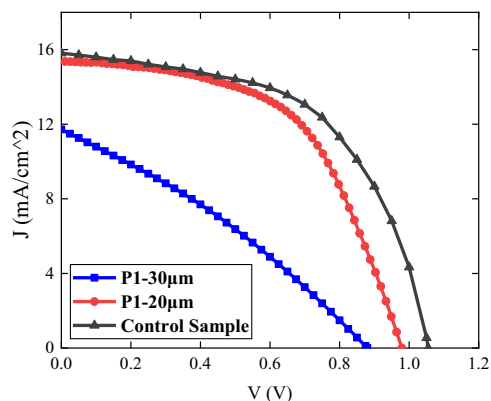
Figure 10. *J–V* curve of the slot-die control sample (black line), champion module fabricated with P1–30 μm (blue line), and champion module fabricated with P1–20 μm (red line). All module performance is averaged to the performance of each cell for comparison with a small-area control sample.
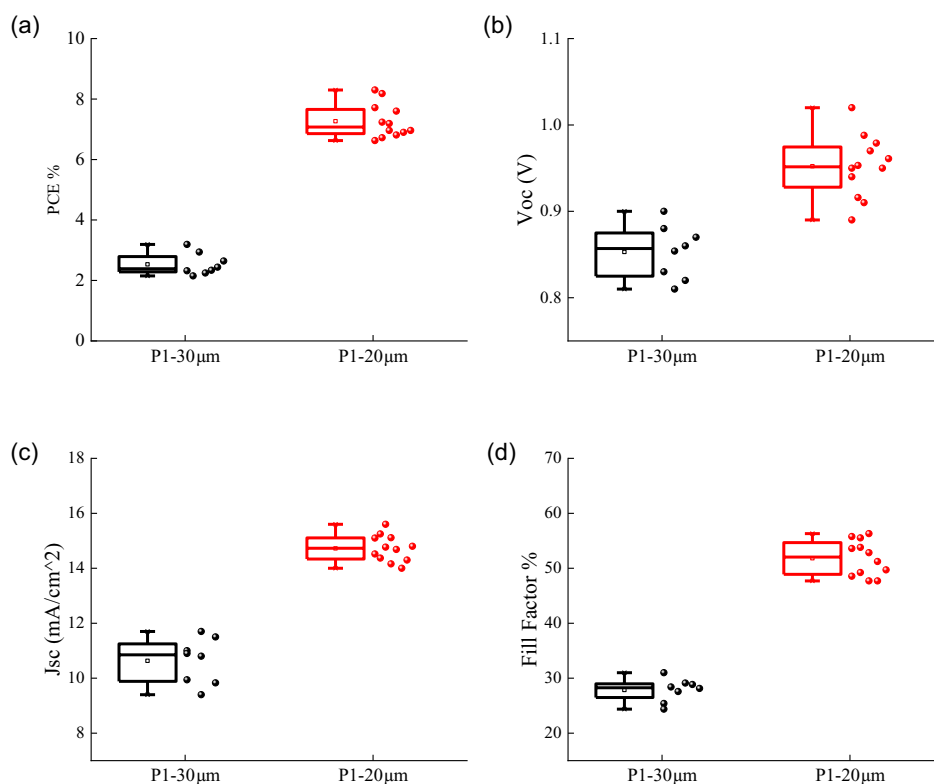
Figure 9. Box chart of a) power conversion efficiency (PCE), b) V_{oc}, c) J_{sc}, and d) fill factor. All module performance is averaged to the performance of each cell for comparison with a small-area control sample.
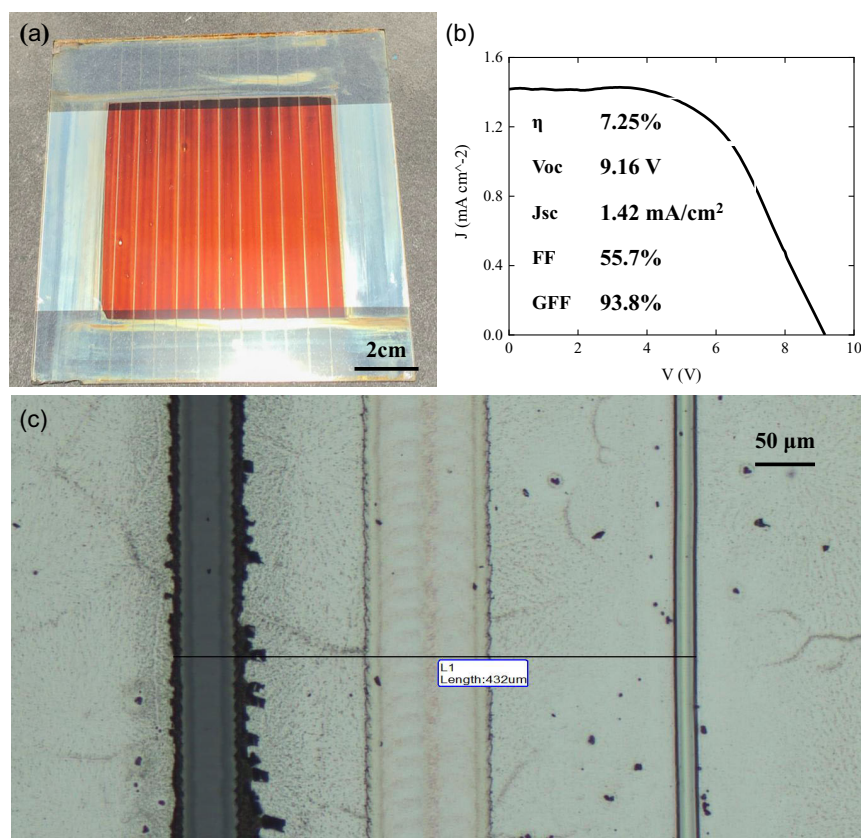
Figure 11. a) Image of large-area perovskite solar modules (PSM). b) *J–V* curve of the module. c) OM image of the dead area.

than the control sample, resulting from the coating defects and internal loss of large cell width (7 mm).

Finally, a large-area module with ten cells was fabricated, and the module's picture is shown in **Figure 11**a. The module exhibited a PCE of 7.2% based on an active area of 46 cm^2, as shown in the *J–V* curve in Figure 11b. OM image of the dead area of the large-area module is shown in Figure 11c. The width of the dead zone is 432 μm which corresponds to an excellent GFF of 93.8%.

3. Conclusion

In this article, we have studied the effects of laser-scribing P1 of FTO films on the coating and crystallization of the perovskite layer during the rapid fabrication process in ambient air with slot-die coating and NIR heating. The redeposition of the ablated material during P1 scribing causes an increase in the surface roughness of FTO film and a decrease in the wettability of FTO film and precursor solutions. The abnormal crystallization of the perovskite layer is also related to the lower-temperature and high-temperature gradient around the P1 line during the NIR heating process. A numerical simulation was performed to verify the analysis. Finally, with the optimized laser parameters, we successfully fabricated a dozen of mini modules with an average PCE of 7.3% and the champion PCE of 8.3% based on an active area of 13.4 cm^2. The largest module showed a PCE of 7.2% on an active area of 46 cm^2 and a GFF of 93.8%.

4. Experimental Section

Material Preparation: Tetramethylammonium hydroxide (TMAOH)-assisted NiO$_x$ precursor solution was prepared as a HTL according to the method reported in Ref. [18]. Briefly, the TMAOH solution was prepared by adding 54 mg TMAOH (>97%, Sigma) to 1 mL ethanol (anhydrous, Fisher Chemical). For NiO$_x$ solution, 74.6 mg (Ni(CH$_3$COO)$_2$)•4H$_2$O (99%, Showa Chemical) was dissolved in 1 mL of ethanol. Then, the solution was stirred at 70 °C for 20 min and added 18 μL ethanolamine (99%, ACROS Organic). Finally, 1 mL NiO$_x$ solution was mixed with 200 μL TMAOH solution. Before the coating process, the NiO$_x$ sol–gel was filtered with 0.22 (m PTFE syringe filters.

MAPbI$_3$ was used as an absorber layer in this study. The 96 mg methylammonium iodide (MAI, STAREK Scientific Co., Ltd.), 276 mg lead iodide (PbI$_2$, 99%, ACROS Organic), and 0.18 mg polyethylene glycol (PEG, M_w 6 k, ACROS Organic) were mixed and then dissolved in the mixture of GBL (99+%, ACROS Organic) and DMSO (99.7+%, ACROS Organic), which is an environment-friendly mixed solvent.[19] *N*-butanol (99.8%, Fisher Chemical) was added to the solution to accelerate the drying and crystallization of perovskite during the NIR heating. The volume ratio of the GBL, DMSO, and n-butanol in the solvent mixture is 1:8:1.

The phenyl-C$_{61}$-butyric acid methyl ester (PC$_{61}$BM, 99.5%, Solenne B.V.) with a concentration of 15 mg mL^{-1} in o-xylene (99%, ACROS Organic) was used as an ETL. A 0.05 wt% tetrabutylammonium hydroxide 30-hydrate (TBAOH, 99%, Sigma–Aldrich) in isopropanol (IPA, 99.5% Extra Dry, ACROS Organic) was used to fabricate WFL, which modifies the band alignment between phenyl-C61-butyric acid methyl ester and Ag.

Slot-Die Coating and NIR Heating: The four functional layers, that is, HTL, perovskite, ETL, and WFL, were deposited on a 12 × 12 cm^2 glass

coated with FTO (7 Ω sq^{-1}, Solaronix, Aubonne, Switzerland) with a semi-automated slot-die coating machine developed by National Taiwan University and E-sun Co. Ltd., in ambient air.[7e,f] NIR lamps were installed for in-line heating processes. Rapid NIR drying and annealing were applied after the deposition of each layer to accelerate the solvent evaporation and complete the crystallization process. The procedure and parameters of the coating and annealing processes can be found in our previous report.[7f]

Laser-Scribing Processes: The laser-scribing system used in this research is co-developed by National Taiwan University and ESUN Co., Ltd (Tainan, Taiwan). The XY stages are driven by linear motors, and the *Z* axis is driven by a servo motor. A charge coupled device camera was used to align the scribing lines with "+" marks on the glass surface. An Nd: YAG 532 nm nanosecond-pulse laser (DCH532-7, Photonics Industries, New Taipei City, Taiwan) with a pulse duration of 7 ns was used for patterning processes. The perovskite layer has a high absorption coefficient to visible light; a 532 nm laser can effectively heat up and remove the perovskite layer with minimum damage to the non-scribing area. A 2*x* object lens was installed to focus the laser beam. This study's patterning processes were performed in the laser-scribing system.

FTO glass was cleaned with ethanol and deionized water and blown dry with nitrogen gas. P1 laser scribing was applied to scribe FTO film. The distance between P1 lines, or cell width, was set as 7 mm. After the slot-die coating of four functional layers and rapid NIR heating, laser scribing was applied for P2. Then, 100 nm thick silver was thermally evaporated as the back electrode. Laser scribing of P3 was applied to isolate the back electrode as the final step to complete the module fabrication. The detail of P2 and P3 scribing process can be found in our previous report.[17] Modules with the size of $4 \times 4 \text{ cm}^2$, which has five cells connected in series, and $7 \times 7 \text{ cm}^2$ with ten cells, were fabricated and measured for PCEs.

Characterization Tools: An optical microscope (OM, DM 500, Leica) was used to observe the scribing line after laser processes. The surface profile around the scribing line was measured with an atomic force microscope (AFM, MultiMode 8, Bruker). EDS (Oxford) analysis coupled with a scanning electron microscope (SEM, JSM-6510, JEOL) was applied to detect the residual element after laser processes. A solar simulator (YSS-150A, Yamashita Denso) with a source meter (Keithley 2410) was used for the PCE measurement. Before each measurement, the light intensity was calibrated to AM 1.5 (100 mW cm^{-2}) with a standard Si solar cell.

Conflict of Interest

The authors declare no conflict of interest.

Data Availability Statement

The data that support the findings of this study are available from the corresponding author upon reasonable request.

[1] J. Jeong, M. Kim, J. Seo, H. Lu, P. Ahlawat, A. Mishra, Y. Yang, M. A. Hope, F. T. Eickemeyer, M. Kim, Y. J. Yoon, I. W. Choi, B. P. Darwich, S. J. Choi, Y. Jo, J. H. Lee, B. Walker, S. M. Zakeeruddin, L. Emsley, U. Rothlisberger, A. Hagfeldt, D. S. Kim, M. Grätzel, J. Y. Kim, *Nature* **2021**, *592*, 381.

[2] D.-N. Jeong, D.-K. Lee, S. Seo, S. Y. Lim, Y. Zhang, H. Shin, H. Cheong, N.-G. Park, *ACS Energy Lett.* **2019**, *4*, 1189.

[3] a) D. K. Mohamad, J. Griffin, C. Bracher, A. T. Barrows, D. G. Lidzey, *Adv. Energy Mater.* **2016**, *6*, 1600994; b) S. Das, B. Yang, G. Gu, P. C. Joshi, I. N. Ivanov, C. M. Rouleau, T. Aytug, D. B. Geohegan, K. Xiao, *ACS Photonics* **2015**, *2*, 680.

[4] Z. H. Wei, H. N. Chen, K. Y. Yan, S. H. Yang, *Angew. Chem. Int. Ed.* **2014**, *53*, 13239.

[5] a) K. Cao, Z. Zuo, J. Cui, Y. Shen, T. Moehl, S. M. Zakeeruddin, M. Grätzel, M. Wang, *Nano Energy* **2015**, *17*, 171; b) A. Priyadarshi, A. Bashir, J. T. Gunawan, L. J. Haur, A. Bruno, Z. Akhter, N. Mathews, S. G. Mhaisalkar, *Energy Technol.* **2017**, *5*, 1866.

[6] a) J. H. Kim, S. T. Williams, N. Cho, C.-C. Chueh, A. K.-Y. Jen, *Adv. Energy Mater.* **2015**, *5*, 1401229; b) Z. Yang, C.-C. Chueh, F. Zuo, J. H. Kim, P.-W. Liang, A. K.-Y. Jen, *Adv. Energy Mater.* **2015**, *5*, 1500328; c) Y. Deng, Q. Dong, C. Bi, Y. Yuan, J. Huang, *Adv. Energy Mater.* **2016**, *6*, 1600372; d) Y. Deng, X. Zheng, Y. Bai, Q. Wang, J. Zhao, J. Huang, *Nat. Energy* **2018**, *3*, 560; e) H. L. Hu, Z. W. Ren, P. W. K. Fong, M. C. Qin, D. J. Liu, D. Y. Lei, X. H. Lu, G. Li, *Adv. Funct. Mater.* **2019**, *29*, 1900092.

[7] a) T. Qin, W. Huang, J.-E. Kim, D. Vak, C. Forsyth, C. R. McNeill, Y.-B. Cheng, *Nano Energy* **2017**, *31*, 210; b) G. Cotella, J. Baker, D. Worsley, F. De Rossi, C. Pleydell-Pearce, M. Carnie, T. Watson, *Sol. Energy Mater. Sol. Cells* **2017**, *159*, 362; c) Y. Galagan, F. Di Giacomo, H. Gorter, G. Kirchner, I. de Vries, R. Andriessen, P. Groen, *Adv. Energy Mater.* **2018**, *8*, 1801935; d) V. Zardetto, F. D. Giacomo, D. Zhang, D. Burgess, W. Verhees, H. Fledderus, I. Dogan, M. Najafi, H. Lifka, Y. Galagan, M. Creatore, G. Coletti, P. Poodt, S. Veenstra, R. Andriessen, presented at *2019 IEEE 46th Photovoltaic Specialists Conference (PVSC)*, IEEE, Piscataway, NJ, June 2019; e) B.-J. Huang, C.-K. Guan, S.-H. Huang, W.-F. Su, *Solar Energy* **2020**, *205*, 192; f) S.-H. Huang, C.-K. Guan, P.-H. Lee, H.-C. Huang, C.-F. Li, Y.-C. Huang, W.-F. Su, *Advanced Energy Materials* **2020**, *10*, 2001567.

[8] a) F. X. Xie, D. Zhang, H. Su, X. Ren, K. S. Wong, M. Grätzel, W. C. H. Choy, *ACS Nano* **2015**, *9*, 639; b) G. M. Kim, T. Tatsuma, *J. Phys. Chem. C* **2016**, *120*, 28933.

[9] a) H.-C. Liao, P. Guo, C.-P. Hsu, M. Lin, B. Wang, L. Zeng, W. Huang, C. M. M. Soe, W.-F. Su, M. J. Bedzyk, M. R. Wasielewski, A. Facchetti, R. P. H. Chang, M. G. Kanatzidis, T. J. Marks, *Adv. Energy Mater.* **2017**, *7*, 1601660; b) H. Tsai, W. Nie, Y.-H. Lin, J. C. Blancon, S. Tretiak, J. Even, G. Gupta, P. M. Ajayan, A. D. Mohite, *Adv. Energy Mater.* **2017**, *7*, 1602159.

[10] a) K. Hwang, Y.-S. Jung, Y.-J. Heo, F. H. Scholes, S. E. Watkins, J. Subbiah, D. J. Jones, D.-Y. Kim, D. Vak, *Adv. Mater.* **2015**, *27*, 1241; b) M. Zhang, H. Yu, J.-H. Yun, M. Lyu, Q. Wang, L. Wang, *Chem. Commun.* **2015**, *51*, 10038; c) L.-L. Gao, C.-X. Li, C.-J. Li, G.-J. Yang, *J. Mater. Chem. A* **2017**, *5*, 1548.

[11] P.-H. Lee, B.-T. Li, C.-F. Lee, Z.-H. Huang, Y.-C. Huang, W.-F. Su, *Sol. Energy Mater. Sol. Cells* **2020**, *208*, 110352.

[12] A. Priyadarshi, L. J. Haur, P. Murray, D. C. Fu, S. Kulkarni, G. C. Xing, T. C. Sum, N. Mathews, S. G. Mhaisalkar, *Energy Environ. Sci.* **2016**, *9*, 3687.

[13] F. Matteocci, S. Razza, F. Di Giacomo, S. Casaluci, G. Mincuzzi, T. M. Brown, A. D'Epifanio, S. Licoccia, A. Di Carlo, *Phys. Chem. Chem. Phys.* **2014**, *16*, 3918.

[14] H. Higuchi, T. Negami, *Jpn. J. Appl. Phys.* **2018**, *57*, 08re11.

[15] A. Fakharuddin, F. Di Giacomo, A. L. Palma, F. Matteocci, I. Ahmed, S. Razza, A. D'Epifanio, S. Licoccia, J. Ismail, A. Di Carlo, T. M. Brown, R. Jose, *ACS Nano* **2015**, *9*, 8420.

[16] a) L. Rakocevic, R. Gehlhaar, T. Merckx, W. Qiu, U. W. Paetzold, H. Fledderus, J. Poortmans, *IEEE J. Photovoltaics* **2017**, *7*, 404; b) A. L. Palma, F. Matteocci, A. Agresti, S. Pescetelli, E. Calabro, L. Vesce, S. Christiansen, M. Schmidt, A. Di Carlo, *IEEE J. Photovoltaics* **2017**, *7*, 1674; c) C. Wang, G. Y. Tan, X. P. Luo, J. Li, X. F. Gao, Y. P. Mo, X. L. Zhang, X. W. Wang, F. Z. Huang, *J. Power Sources* **2020**, *466*, 228321; d) A. Lemke, D. Ashkenasi, H. J. Eichler, *Phys. Procedia* **2013**, *41*, 769; e) P. Kubis, N. Li, T. Stubhan, F. Machui, G. J. Matt, M. M. Voigt, C. J. Brabec, *Prog. Photovoltaics* **2015**, *23*, 238.

[17] B.-Q. Lin, C.-P. Huang, K.-Y. Tian, P.-H. Lee, W.-F. Su, L. Xu, *Int. J. Precis. Eng. Manuf.* **2022**.

[18] M.-H. Jao, C.-C. Cheng, C.-F. Lu, K.-C. Hsiao, W.-F. Su, *J. Mater. Chem. C* **2018**, *6*, 9941.

[19] S.-H. Huang, K.-Y. Tian, H.-C. Huang, C.-F. Li, W.-C. Chu, K.-M. Lee, Y.-C. Huang, W.-F. Su, *ACS Appl. Mater. Interfaces* **2020**, *12*, 26041.

[20] a) X. Liu, D. Du, G. Mourou, *IEEE J. Quantum Electron.* **1997**, *33*, 1706; b) A. L. Palma, *Sol. RRL 19*, 1900432; c) G. Mincuzzi, A. L. Palma, A. Di Carlo, T. M. Brown, *ChemElectroChem* **2016**, *3*, 9.

[21] a) B. N. Chichkov, C. Momma, S. Nolte, F. von Alvensleben, A. Tünnermann, *Appl. Phys. A* **1996**, *63*, 109; b) C. McDonnell, D. Milne, H. Chan, D. Rostohar, G. O'Connor, *Opt. Lasers Eng.* **2016**, *80*, 73.